

# Self-assembled conjugated polymer–surfactant–silica mesostructures and their integration into light-emitting diodes†

E. Dovgolevsky,<sup>a</sup> S. Kirmayer,<sup>a</sup> E. Lakin,<sup>a</sup> Y. Yang,<sup>b</sup> C. J. Brinker<sup>b</sup> and G. L. Frey<sup>\*a</sup>

Received 28th August 2007, Accepted 12th November 2007

First published as an Advance Article on the web 29th November 2007

DOI: 10.1039/b713170d

A self-assembly process for the preparation of functional mesoscopically ordered semiconducting polymer–silica nanocomposite thin films is reported. The nanocomposites are prepared by introducing pre-synthesized semiconducting polymers into a tetrahydrofuran (THF)–water homogeneous sol solution containing silica precursor species and a surface-active agent. Depending on the concentration of the surface-active agent, it was possible to prepare materials with three different types of mesostructural order: i) a 2D hexagonal mesophase silica with conjugated polymer guest species incorporated within the hydrophobic cylinders organized in domains aligned parallel to the substrate surface plane; ii) a lamellar mesophase silica with the layers oriented parallel to the substrate surface and the conjugated polymer guest species incorporated in the hydrophobic layers; or iii) an apparent intermediate phase consisting of a mixture of the hexagonal and lamellar phases in addition to worm-like aggregates with no appreciable orientational order. The continuous through-film conductive pathway provided by the intermediate phase has allowed the integration of ordered semiconducting polymer–silica nanocomposites into opto-electronic devices. By comparison, the lamellar mesostructure prevents through-film conduction, with the result that no light emission occurs. Blue-, green- and red-emitting diodes comprising blue-emitting poly(9,9-dioctylfluorenyl-2,7-diyl) (PFO), green-emitting poly(9,9-dioctylfluorenyl-2,7-diyl)-*co*-1,4-benzo-(2,1',3)-thiadiazole (F8BT), and red-emitting poly[2-methoxy-5(2'-ethyl-hexyloxy)-1,4-phenylenevinylene] (MEHPPV) confined within the 2D hexagonal silica nanostructure were fabricated with luminances of *ca.* 3 cd m<sup>-2</sup> at 15 V. Device performances provide criteria for optimizing the selection of synthesis chemistries, processing conditions, compositions, and structures, for light-emission properties sought.

## Introduction

Conjugated polymers have been the subject of extensive academic and industrial research efforts due to their promising potentials for use as active layers in electronic and opto-electronic devices, such as light-emitting diodes,<sup>1,2</sup> field-effect transistors (FETs),<sup>3,4</sup> lasers,<sup>5</sup> photodiodes<sup>6</sup> and solar cells.<sup>7,8</sup> In these various applications it has been found that, in addition to the intrinsic chemical properties of the polymers and additives, the device performance is strongly dependent on the morphology of the film in which the polymer is cast, which can be influenced further by incorporation into a suitable host matrix. Therefore, attaining control over the chemical composition, morphology and hierarchical structure in the polymer or composite film is expected to enhance device performance and enable the design and fabrication of new types of devices.

The influence of film morphology and interfacial interactions on the mechanical properties of many composite

materials based on *conventional* polymers are well-known.<sup>9</sup> Composite materials are generally designed to enhance or exhibit properties and functions that are unattainable from the individual chemical species or their phases. Polymer–inorganic composites harness the good processability and low density of the polymer component, in combination with the high strength, stiffness, thermal stability, and mechanical durability of the inorganic component. Consequently, synthetic approaches have been developed to control the polymer–inorganic solution and processing chemistries, their physicochemical interactions, and their hierarchical architectures at molecular and mesoscale levels towards specific applications.<sup>10–12</sup>

In this study, polymer–inorganic guest–host composite materials are designed, synthesized, characterized, and integrated into opto-electronic devices. The device performances confirm the successful design and synthesis of the nanocomposites and yield deep insight into the molecular and electronic processes of the materials. Such understanding provides important feedback for optimizing the synthesis chemistry and properties of novel functional conjugated polymer–inorganic nanocomposite materials.

Depending upon the nature of the association between the inorganic and polymeric components, nanocomposites can be classified into two categories: one in which the inorganic material (*e.g.*, nanoparticles, colloids, polyoxometalates) is embedded in a polymeric matrix,<sup>13</sup> and a second, where

<sup>a</sup>Department of Materials Engineering, Technion – Israel Institute of Technology, Haifa 32000, Israel

<sup>b</sup>Department of Chemical and Nuclear Engineering, University of New Mexico and Sandia National Laboratory/UNM Advanced Materials Lab, Albuquerque, NM 87106, USA

† Electronic supplementary information (ESI) available: The absorption spectra of PFO-incorporated Brij-56–silica, and PFO–PEO–silica films, compared to those of pristine PFO polymer films prepared by dip-coating and casting. See DOI: 10.1039/b713170d

organic polymers are confined within an inorganic template.<sup>14</sup> Incorporation of polymers into well-defined channels of an insulating mesoporous inorganic scaffold offers control over the conformation of individual polymer chains, chain–chain stacking, and interfacial interactions with the scaffold “walls”, while providing environmental isolation. Furthermore, highly ordered (nano)engineered voids of an inorganic matrix can be used to induce alignment and preferred orientational ordering of the polymer chains.

Organic-in-inorganic composites present several advantages as optical materials including: mild synthesis conditions, simple processability, mechanical robustness, and most importantly, the ability to tailor the optical properties through host–guest material selection and control of organic–inorganic interactions on a molecular level. Optically responsive dye-incorporated-silica-based hybrid materials have been suggested for fundamental studies such as the spectroscopy of isolated dye molecules in a sol–gel matrix, energy transfer in solids, and the following of the sol–gel process *in situ* via luminescent probes.<sup>15–19</sup> Furthermore, materials with organic dye species included in mesostructured inorganic host matrices, such as silica or zirconia, have shown improved combinations of optical, mechanical, and thermal properties for photochromic, optical limiting, sensor, and laser applications.<sup>15,20,21</sup>

Electronic and opto-electronic applications, however, require that a continuous conductive pathway through the material be present to support charge transport. Boilot and co-workers reported the use of organic–inorganic composites prepared from silane precursors modified with hole- or electron-transporting units and light-emitting species.<sup>22</sup> In this system, the chromophores were covalently bound to the amorphous conductive inorganic framework. A film of this hybrid material sandwiched between indium–tin oxide (ITO) and a cathode produced electroluminescence under forward bias. This light-emitting diode (LED) device exploited sol–gel chemistry for the synthesis of an amorphous organic–inorganic hybrid material, but without self-organization into ordered mesostructures.

The use of orientationally ordered mesostructured materials for controlling the optical and electrical properties of *semiconducting* polymers was first demonstrated for a conjugated polymer–mesoporous nanocomposite.<sup>23–25</sup> In these studies, a semiconducting polymer, poly[2-methoxy-5(2'-ethyl-hexyloxy)-1,4-phenylenevinylene] (MEH-PPV), was infiltrated into the channels of a pre-formed hexagonal mesoporous silica-host. The architecture of the material allowed the authors to quantify the roles of *interchain* and *intrachain* energy transfer in conjugated polymers.<sup>24</sup> Infiltration of polythiophene into a mesoporous titania scaffold for the preparation of photovoltaic devices has also been attempted.<sup>26</sup> Polymer infiltration, however, can be difficult to control because it depends on both partitioning of the polymer from the solvent and reptation into the pore channels, which can be slow due to diffusion limitations. A distribution of polymer chain environments may therefore exist depending on whether the conjugated polymer guest species are fully incorporated, partially incorporated or not incorporated (estimated to be ~20%) in the mesoporous inorganic host.<sup>23–25</sup> For such heterogeneous distributions, accompanying broad distributions of electronic

and optical properties may result that are also challenging to control and optimize. Furthermore, the reptation of polymer chains through the entire micron-thick porous films necessary for device operation, if possible, may require long processing times and elevated temperatures.<sup>23</sup>

In another approach, semiconducting polymers were fully incorporated into a silica scaffold by *in situ* polymerization.<sup>27–30</sup> Although the insertion of reactive monomers into the silica scaffold is relatively simple, *in situ* polymerization often results in high contamination levels of unreacted precursor monomers and leaving groups due to modest extents of polymerization and sluggish molecular diffusion from the inorganic mesopores, respectively. Low-polymerization yields tend to result in the presence of non-conductive segments in the polymer chains that impede or altogether suppress carrier transport in the corresponding devices.

An alternative approach is to incorporate high-molecular-weight conjugated polymer species *during* synthesis and processing of the self-assembling inorganic–surfactant mesostructured host. One way to do so is to prepare thin films of mesostructured silica by evaporation-induced self-assembly (EISA). In this process, thin films are deposited from an EtOH–water solution containing silica precursor and surfactant species initially below the critical micelle concentration (cmc) of the solution.<sup>31,32</sup> Preferential evaporation of ethanol during dip-coating concentrates the non-volatile surfactant and silica species, which under the right conditions will co-assemble. Progressively increasing concentrations tend to promote the formation of highly ordered silica–surfactant mesophases, which are fixed by silica polymerization. The EISA process provides a simple coating procedure and is advantageous for the deposition of conjugated polymer–silica nanocomposite films in view of their integration into opto-electronic applications.

Semiconducting polymers, however, are not soluble in polar solvents and therefore not amenable for introduction into sol–gel precursor solutions. As a consequence, one must select a solvent that is compatible with both cross-linkable inorganic precursor species and the functional semiconducting polymer guests to circumvent undesirable macrophase separation. Moreover, because solid-state effects greatly influence the optical and electrical properties of conjugated polymers, the selected solvent must be sufficient to avoid aggregation and  $\pi$ – $\pi$  stacking of the semiconducting polymer, which restricts substantially the options available. Water-soluble dye molecules are abundant, and therefore, preparation of optically-responsive dye-incorporated mesostructured silica does not suffer solubility limitations. Opto-electronic properties, however, require also a continuous conductive pathway for carrier mobility. Whereas through-film conductivity is generally unattainable in unstructured dye–silica blends, conjugated polymers incorporated in mesostructured silica matrices can yield robust opto-electronic properties, depending on the connectivity and alignment of the mesochannels.

An important consideration for the selected solvent is that it must solubilize both the hydrophobic semiconducting polymer and the silica precursor species. A useful means for estimating the solubility of a polymer in a solvent is the squared difference of the Hildebrand parameters of the solvent and solute

$(\delta_{\text{solvent}} - \delta_{\text{solute}})^2$ . Similar  $\delta$  values for the solvent and polymer solute indicate good mutual solubility. For example, polyfluorene has a  $\delta$  value of approximately 9.1 to 9.3 ( $\text{cal cm}^{-3}$ )<sup>1/2</sup>, compared to THF ( $\delta_{\text{THF}} = 9.1$ ) and chloroform ( $\delta_{\text{CHCl}_3} = 9.1$ ), which are known to be good solvents for polyfluorene; toluene ( $\delta_{\text{Tot}} = 8.9$ ) and chlorobenzene ( $\delta_{\text{CB}} = 9.5$ ) are moderately good solvents; while cyclohexane ( $\delta_{\text{CH}} = 8.2$ ) and dichloroethane ( $\delta_{\text{DCE}} = 9.8$ ) are moderately poor and very poor, respectively.<sup>33</sup> In addition to the Hildebrand solubility parameter, it is important to also consider the polymer–solvent interactions. For example, the  $\delta$  value of MEH-PPV is similar to that of THF and chlorobenzene, however, MEH-PPV chains tend to form tight coils with short conjugation lengths and restricted aggregation in non-aromatic organic solvents, such as THF, while maintaining an open and straight conformation with a longer mean conjugation length that promotes aggregation in aromatic chlorobenzene solutions.<sup>34</sup> These polymer aggregates may reside in the film during the slow evaporation of relatively high boiling-point solvents, like chlorobenzene, and result in macroscopically phase-separated domains of the conjugated polymer in the silica matrix.<sup>34,35</sup> Rapid evaporation of a volatile solvent, such as THF, on the other hand, avoids segregation of the semiconducting polymer, though must be balanced to permit self-assembly of the structure-directing species. High solvent volatility and accompanying low viscosity is also essential for the deposition of thin films using the EISA method.<sup>36</sup> Accordingly, the preparation of transparent mesostructured organosilica in host polymer membranes by *in situ* growth in THF solution was very recently reported, although no optical guest species were incorporated.<sup>37</sup>

Here, we describe a robust new synthetic approach for the preparation of mesoscopically ordered semiconducting polymer–silica nanocomposite thin films through the co-assembly of silica precursor species, surfactant, and pre-polymerized semiconducting polymers from a homogeneous THF–water solution. In this process, the commercially available hydrophobic semiconducting polymers are, for the first time, incorporated into the mesostructured silica upon its formation. The optical and electrical properties of the conjugated polymers are maintained upon incorporation, enabling their utilization in opto-electronic applications. A non-ionic surfactant, Brij-56, was used in this study because it is known to direct the deposition of a variety of phases in the conventional sol–gel process, and will not contribute parasitic ionic currents to devices comprising the mesostructured films.<sup>38,39</sup> However, the approach reported here is general and can be easily implemented to a variety of different non-ionic surfactants, inorganic host matrices and conjugated polymers. Encapsulation of the conjugated polymer species in the mesostructured host could also offer improved mechanical and environmental stability against external chemical and mechanical damage.<sup>40–42</sup>

## Experimental

### Materials

Tetraethylorthosilicate (TEOS), hydrochloric acid (HCl) and tetrahydrofuran (THF) (Aldrich) were used as the silica precursor, catalyst and solvent, respectively. An amphiphilic

non-ionic polymer, Brij-56<sup>TM</sup> poly(oxyethylene) cetylerether ( $\text{CH}_3(\text{CH}_2)_{15}-(\text{OCH}_2\text{CH}_2)_{10}-\text{OH}$ ) (Aldrich) was used as structure-directing agent. Three semiconducting polymers (American Dye Source) were used: poly((9,9-dioctylfluorenyl-2,7-diyl)) (PFO,  $M_w = 80\,000$ ), poly((9,9-dioctylfluorenyl-2,7-diyl)-*co*-1,4-benzo-(2,1',3)-thiadiazole) (F8BT,  $M_w = 15\,000$ ), and poly(2-methoxy-5-(2-ethyl hexyloxy)-1,4-phenylenevinylene) (MEH-PPV,  $M_w = 480\,000$ ).

### Synthesis of silica sol

In a typical synthesis, a THF-rich–water sol solution was prepared from TEOS, Brij-56, HCl catalyst and a semiconducting polymer, either PFO, F8BT or MEH-PPV. First, 15 ml of TEOS were prehydrolyzed in a solution containing 6 ml of 0.07 N HCl and 75 ml of THF and stirred vigorously at room temperature for 1 h. Then, to 1.5 ml of this solution, either 0.237, 0.178 or 0.089 g of Brij-56 surfactant were added so that the surfactant concentration ( $c_0$ ) in the sol solution is 8, 6, or 3 wt%, respectively. Finally, 1.5 ml of this sol solution was then mixed with 2.25 ml of a THF filtered solution containing either 5.6 mg MEH-PPV or F8BT, or 3.4 mg PFO. The lower PFO concentration is due to its lower solubility in the sol solution compared to that of F8BT and MEH-PPV. For example, the final mole ratios in the semiconducting polymer–6 wt%-Brij56–silica sol solution prior to dip-coating are: 1 TEOS : 40.27 THF : 4.96 H<sub>2</sub>O :  $6.3 \times 10^{-3}$  HCl :  $4.13 \times 10^{-5}$  PFO or  $3.57 \times 10^{-4}$  F8BT or  $1.11 \times 10^{-5}$  MEH-PPV : 0.249 Brij-56, respectively. The semiconducting polymer–Brij-56 molar ratio was kept constant in all precursor solutions. For example, the semiconducting polymer–3 wt%-Brij-56–silica sol solution was prepared following the procedure detailed above for the semiconducting polymer–6 wt%-Brij-56–silica sol solution, adding the same volume of THF with only half of the semiconducting polymer concentration.

### Thin film preparation

Nanocomposite thin films were prepared by dip-coating at a rate of 20 ipm, spin-coating at 1500–2000 rpm, or drop-casting in ambient atmosphere (23–25 °C, and 75–85% of relative humidity) on <100> single-crystal Si wafers, glass slides, polyimide films or ITO substrates. All deposited thin films were continuous, uniform and crack-free as evident from high-resolution scanning electron microscopy.

Conjugated polymer loadings of the nanocomposite films were estimated by dissolving the product films in small amounts of THF under vigorous stirring. The concentration of the polymer in the solution was determined by optical absorption spectroscopy, and the substrate weighed prior to and after film removal, from which conjugated polymer concentrations in the films was estimated.

### Characterization

X-Ray diffraction (XRD) measurements were performed on a Bede D3 X-ray diffractometer equipped with an 18 kW Rigaku rotating anode generator at  $\theta$ – $2\theta$  scan mode in reflection geometry. A highly monochromatized  $\text{CuK}_{\alpha 1}$  line with

$\lambda = 1.5406 \text{ \AA}$  was selected from the primary X-ray beam by means of two channel-cut (220) Si crystals. Small-angle X-ray scattering measurements (SAXS) were performed using a small-angle diffractometer (Bruker Nanostar, KFF CU 2 K-90) with  $\text{CuK}_\alpha$  radiation with  $\lambda = 1.542 \text{ \AA}$ . Pinhole collimation yielding a beam  $100 \mu\text{m}$  in diameter and a  $10 \times 10 \text{ cm}^2$  two-dimensional position-sensitive wire detector positioned  $65 \text{ cm}$  behind the sample were used. The patterns were recorded using an acceleration voltage of  $40 \text{ kV}$  and acceleration current of  $30 \text{ mA}$ . The polyimide substrates were vertically located in the SAXS diffractometer and patterns were recorded in transmission mode with fixed incidence angle  $\alpha$  (the angle between the incident beam and the sample surface) of approximately  $2^\circ$ , as illustrated schematically in Fig. 1. This configuration, referred to as “glancing incidence”, mimics the “grazing incidence” technique where the X-ray beam is incident at nearly the critical angle.<sup>38</sup> The 2D SAXS “glancing incidence” scattering geometry shows diffracted intensity exclusively out-of-the-film-plane.<sup>38,43</sup> To elucidate the orientation of the films, 2D SAXS measurements were performed by rotating the film horizontally with respect to the X-ray beam from the coating direction by  $90^\circ$ .<sup>39</sup> High-resolution scanning electron microscopy (HRSEM) measurements were carried out using a LEO Gemini 982 field emission gun SEM (FEG-SEM). Transmission electron microscopy (TEM) measurements were performed using a JEOL JEM 2010 transmission electron microscope operated at  $200 \text{ keV}$ . TEM samples were prepared by scratching the thin films and directly dispersing the film fragments onto holey carbon copper grids. Absorption spectra were taken using a Varian Cary 100 Scan UV-vis spectrophotometer. Photoluminescence spectra were collected at room temperature with a Varian Cary Eclipse fluorimeter using excitation wavelengths of  $395 \text{ nm}$  for PFO and  $481 \text{ nm}$  for F8BT and MEH-PPV.

### Device fabrication and measurements

Devices were prepared by spin-coating a  $100 \text{ nm}$  poly(ethylenedioxythiophene)–poly(styrene sulfonic acid) (PEDOT:PSS) layer on a  $12 \times 12 \text{ mm}^2$  ITO substrate, followed by a  $200^\circ \text{C}$  heat treatment for  $2 \text{ h}$  under inert conditions. The  $110\text{--}210 \text{ nm}$  thick nanocomposite layer was deposited by dip-coating the

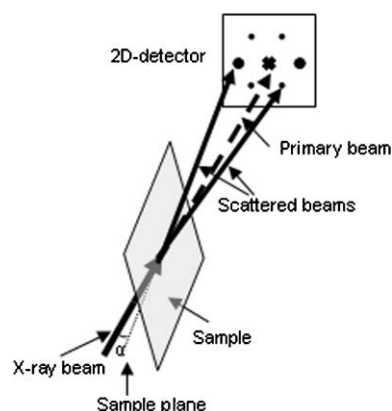


**Fig. 1** A schematic diagram of the experimental configuration used for glancing incidence small-angle X-ray scattering measurements.

PEDOT:PSS-coated substrate in the sol solution. The device was completed by thermally evaporating eight  $\text{Ca}(30 \text{ nm})\text{--Al}(150 \text{ nm})$  cathode contacts (pixel size of  $1 \times 3 \text{ mm}^2$ ). LED performances were measured using an Agilent 4155C semi-conducting parameter analyzer under inert conditions. It is worth noting that the device characteristics are presented in terms of applied bias (and not field) because all films used in this study, pristine polymer or nanocomposites, are of similar thicknesses ( $100\text{--}150 \text{ nm}$ ).

## Results and discussion

### Nanocomposite synthesis and structure characterization

The nanocomposites in this study were prepared by introducing pre-synthesized hydrophobic semiconducting polymers into a THF–water homogeneous sol solution containing silica precursor species and a surface-active amphiphilic agent. The surfactants used were amphiphilic and non-ionic, composed of hydrophobic and hydrophilic blocks. In the EISA process, evaporation of the THF concentrates the surfactant, which promotes the self-assembly of micellar aggregates, with the semiconducting polymer associated with the hydrophobic surfactant block. Evaporative film deposition concentrates the surfactant micelles and directs their assembly into ordered three-dimensional mesophases accompanied by polycondensation of the silica precursor. The choice of surfactant concentration significantly influenced the resulting mesostructure, while the choice of the semiconducting polymers, PFO, F8BT or MEH-PPV, did not, for the concentrations and conditions examined. Combined 1D X-ray, 2D-SAXS and TEM measurements indicated that the Brij-56-directed nanocomposite films adopt either a lamellar mesophase or a 2D hexagonal structure.

A 2D hexagonal mesostructure, with domains of cylinders aligned parallel to the substrate, was found for the Brij-56-directed silica nanocomposite films spun, dip-coated or cast from the  $3 \text{ wt}\%$  Brij-56 in THF sol solution (with no conjugated polymer in the sol solution). In Fig. 2A, the 2D glancing-incidence SAXS pattern from a  $3 \text{ wt}\%$  Brij-56-directed mesostructured silica film shows sharp, intense (100) spots normal to the film plane, and weaker (010) reflections. This pattern reflects a highly regular 2D hexagonal structure with  $d$ -spacing of  $4.99 \text{ nm}$ , preferentially oriented with the cylinder  $a$ -axes parallel to the film plane and the  $c$ -axes randomly oriented within the film plane,<sup>39,44</sup> as schematically illustrated in Fig. 2B. The random orientation of the  $c$ -axis was further confirmed by rotating the film  $90^\circ$  horizontally with respect to the X-ray beam. The intensity of the spots was maintained upon film rotation (not shown), indicating that the dip-coating process did not induce a preferred orientation of the cylinders in the withdrawal direction.<sup>39</sup> The film-forming process and attendant constraint of the substrate, however, induces a distortion in the hexagonal symmetry with a contraction along the direction normal to the film plane, as evident from the slightly smaller  $d$ -space between (100) planes compared to that between (010) planes. This well-documented anisotropic shrinkage in hexagonal dip-coated films is due to the drying and polycondensation of the silica network during substrate withdrawal and aging.<sup>44,45</sup> The 2D

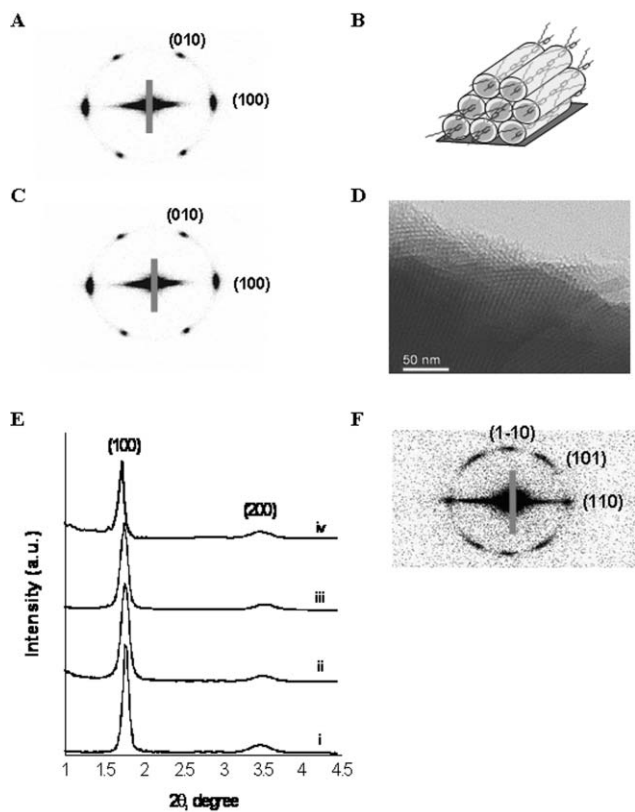


**Fig. 2** (A) The 2D-SAXS pattern of a 3 wt% Brij-56-directed silica nanocomposite film (the film plane is indicated by the vertical grey line as explained in the Experimental), (B) A schematic illustration of the 2D hexagonal domains with cylindrical aggregates aligned parallel to the substrate. (C) The 2D SAXS pattern of a 3 wt% Brij-56-directed PFO-incorporated silica nanocomposite film. (D) A TEM image of the 2D hexagonal domains in a 3 wt% Brij-56-directed silica nanocomposite film, showing orientations parallel to the cylinder axis. (E) 1D X-ray patterns of a 3 wt% Brij-56-directed mesostructured silica film (line i), and 3 wt% Brij-56-directed nanocomposite films incorporated with: red-emitting MEH-PPV (line ii), blue-emitting PFO (line iii), and green-emitting F8BT (line iv). (F) The 2D-SAXS pattern of a cubic 3 wt% Brij-56-directed silica nanocomposite spun film measured near the film edge.

glancing-incidence SAXS pattern (Fig. 2A) also shows very weak continuous diffraction arcs that are superimposed on the hexagonal spot pattern, attributed to the spatial correlation of worm-like cylindrical aggregates during their pre-positioning into a highly ordered hexagonal arrangement.<sup>46–48</sup>

Transmission electron microscopy (TEM) images (Fig. 2D) provide further evidence for the presence of the 2D hexagonal domains showing orientations parallel to the cylinder axes.<sup>39,44</sup> The spacing between fringes is approximately 5 nm, which is in good agreement with the unit cell parameters determined from the SAXS data. The 1D X-ray diffraction pattern of the 3 wt% Brij-56-directed silica (with no semiconducting polymer), presented in Fig. 2E, line i, is also in good agreement with the 2D-SAXS pattern. Two peaks, assigned to the (100) and (200) reflections of a highly ordered hexagonal mesostructure with a  $d$ -spacing of 4.99 nm, and the absence of the (110) reflection, confirm the preferentially oriented hexagonal structure with the cylinders aligned parallel to the film plane.<sup>39,44</sup>

It is worthy to note that a cubic mesophase was also identified in the SAXS patterns of thick films ( $\sim 230$  nm) prepared by spin-coating from the 3 wt% Brij-56-silica sol solutions without and with semiconducting polymers as shown in Fig. 2F. The sharp intense eight spots correspond to the (110), (101), and (1–10) reflections of a body-centered cubic ( $Im3m$ ) structure with  $d$ -spacing of 5.45 nm.<sup>49</sup> The cubic mesophase is oriented with the (110) planes parallel to the substrate, and is slightly distorted due to the contraction along the direction normal to the film plane,<sup>49</sup> similar to the distortion observed for the 2D hexagonal structure.<sup>44,45</sup>

Incorporation of conjugated polymers into the 3 wt% Brij-56 THF sol solution does not alter the main 2D-hexagonal structure of the resulting films, as evident from the 2D-SAXS (Fig. 2C) and 1D X-ray (Fig. 2E) patterns of 3 wt% Brij-56-directed MEH-PPV, PFO, or F8BT-incorporated mesostructured silica films. The patterns of all conjugated polymer-incorporated films, despite the type and molecular weight of the conjugated polymer, show strong and sharp (100) and (200) reflections of a 2D hexagonal mesostructure with a  $d$ -spacing of approximately 5.05–5.14 nm, which is slightly larger than that obtained for non-conjugated polymer-incorporated silica film. The  $d$ -spacing values calculated from the 1D X-ray patterns, with and without conjugated polymers incorporated (Fig. 2E), are listed in Table 1. The weak continuous diffraction arcs of worm-like cylindrical micelles domains are also noticeable in the SAXS patterns of all semiconducting polymer-incorporated hexagonal films. However, the high polydispersity of the incorporated conjugated polymer guest species, along with the altered hydrophobic–hydrophilic interactions, results in diminished overall order of the hexagonal system compared to that of the non-intercalated mesostructured Brij-56-silica host as evident from the less intense and broader SAXS reflections upon conjugated polymer incorporation.

A highly ordered lamellar mesophase was found for 8 wt% Brij-56-directed silica nanocomposite films cast from THF, with and without a conjugated polymer guest species incorporated, as shown in Fig. 3A and 3C, respectively. The two strong reflections, in both patterns, indexed as (001) and (002), are exclusively out-of-the-film-plane (see Experimental and Fig. 1), and are consistent with a lamellar film structure that is aligned parallel to the substrate,<sup>44</sup> a schematic diagram of which is shown in Fig. 3B. The TEM image of a PFO-containing lamellar nanocomposite film (Fig. 3D) shows layered features typical of a lamellar silica mesostructure, in good agreement with the X-ray results. The 1D X-ray patterns of 8 wt% Brij-56-directed silica film with either no semiconducting polymers incorporated or otherwise identical films containing MEH-PPV, PFO, or F8BT are shown in Fig. 3E lines i, ii, iii, and iv. All of these patterns are consistent with the 2D-SAXS data, showing (001) and (002) reflections, respectively, of a highly ordered lamellar mesostructure with a basal spacing of  $\sim 5.30$  nm.<sup>44</sup> Incorporation of the conjugated polymers does not swell the lamellar structure, but decreases the overall order of the lamellar system, evident from the lower intensity of the polymer-incorporated films X-ray reflections compared to that of the non-intercalated lamellar silica host. The basal-spacing values calculated from the 1D X-ray

**Table 1** Hexagonal lattice parameters and lamellar basal spacing values of the 3, 6 and 8 wt% Brij-56-directed mesostructured silica films, and 3, 6 and 8 wt% Brij-56-directed semiconducting polymer-incorporated silica mesostructured films, calculated from the 1D X-ray patterns presented in Fig. 2E, 3E and 4E

Amount of Brij-56 in sol/wt%	Semiconducting polymer	$2\theta$ (hexagonal), (100)/(200) degree	$d$ -spacing (hexagonal) (100)/(200)/Å	$2\theta$ (lamellar) (001)/(002) degree	$d$ -spacing (lamellar) (001)/(002)/Å	Mesophase
3	None	1.77/3.36	49.92/26.30	—	—	Hexagonal
3	MEHPPV	1.75/3.50	50.49/25.25	—	—	Hexagonal
3	PFO	1.75/3.50	50.49/25.25	—	—	Hexagonal
3	F8BT	1.72/3.44	51.37/25.69	—	—	Hexagonal
6	None	1.77/3.36	49.92/26.30	1.66/3.32	53.22/26.62	Mixed
6	MEHPPV	1.77/3.36	49.92/26.30	1.68/3.36	52.59/26.29	Mixed
6	PFO	1.73/3.46	51.07/25.91	1.65/3.30	53.54/26.77	Mixed
6	F8BT	1.76/3.52	50.20/25.10	1.65/3.30	53.54/26.77	Mixed
8	None	—	—	1.67/3.34	52.91/26.46	Lamellar
8	MEHPPV	—	—	1.67/3.34	52.91/26.46	Lamellar
8	PFO	—	—	1.66/3.32	53.22/26.62	Lamellar
8	F8BT	—	—	1.65/3.30	53.54/26.77	Lamellar

patterns of the 8 wt% Brij-56-directed silica films, with and without conjugated polymer incorporation, are listed in Table 1.

At an intermediate concentration of the structure-directing surfactant, 6 wt% Brij-56 in the THF-rich sol solution with and

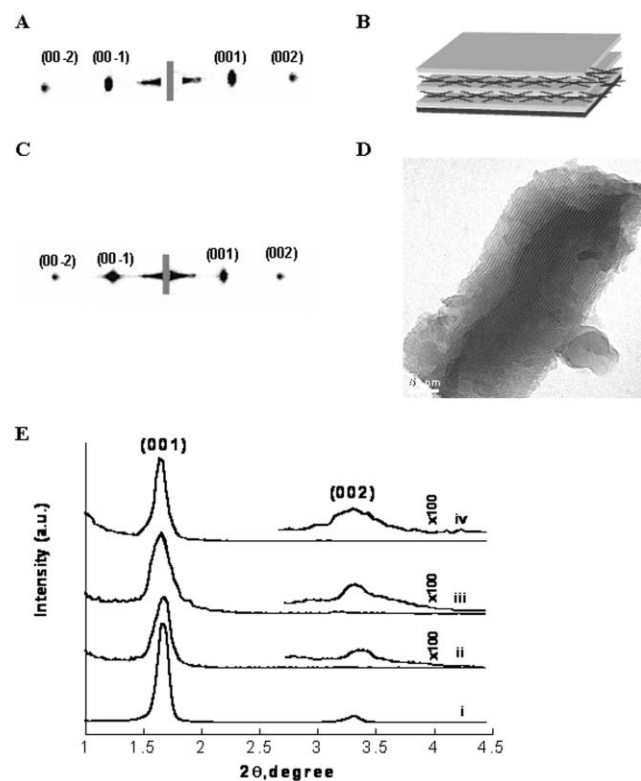


**Fig. 3** (A) The 2D-SAXS pattern of a 8 wt% Brij-56-directed silica nanocomposite film (the film plane is indicated by the vertical grey line as explained in the Experimental). (B) A schematic illustration of the lamellar mesostructure with the lamellae oriented parallel to the substrate. (C) The 2D-SAXS pattern of an 8 wt% Brij-56-directed PFO-incorporated silica nanocomposite film. (D) A TEM image of the lamellar 8 wt% Brij-56-directed mesostructured silica film. (E) 1D X-ray patterns of 8 wt% Brij-56-directed mesostructured silica film (line i), and 8 wt% Brij-56-directed nanocomposite films incorporated with: red-emitting MEH-PPV (line ii), blue-emitting PFO (line iii), and green-emitting F8BT (line iv).

without a conjugated polymer guest species, a mixture of the 2D hexagonal and the lamellar mesostructures is obtained. The 2D-SAXS pattern of the 6 wt% Brij-56-directed mesostructured silica films, Fig. 4A, shows the same intense (100) and weaker (010) reflections obtained for the hexagonal 3 wt% Brij-56-directed mesostructured silica films (Fig. 2A),<sup>39,44</sup> together with the (001) and (002) reflection obtained for the lamellar 8 wt% Brij-56-directed mesostructured silica films (Fig. 3A).<sup>44</sup> In addition to the mixture of the hexagonal and lamellar reflections, the 2D-SAXS pattern also shows significant amounts of the disordered worm-like cylindrical domains, schematically illustrated in Fig. 4B. The presence of the worm-like phase is evident from the strong diffraction arcs superimposed on the hexagonal and lamellar spot pattern.

The mixture of phases is also obtained for the conjugated polymer-incorporated 6 wt% Brij-56-directed silica nanocomposite films. Fig. 4C shows the presence of the mixed phases in the 2D-SAXS pattern of the PFO-incorporated 6 wt% Brij-56-directed silica nanocomposite films. Similar patterns were obtained for F8BT- and MEH-PPV-incorporated 6 wt% Brij-56-directed silica nanocomposite films (not shown). In summary, all 6 wt% Brij-56-directed silica nanocomposite films, without and with conjugated polymer, appear to consist of a mixture of three mesostructures: i) 2D hexagonal domains with cylindrical orientations predominantly parallel to the substrate, as shown in the TEM image (Fig. 4D); ii) worm-like aggregates without appreciable orientational order; and iii) lamellar regions with the lamellae parallel to the substrate.

The combination of the hexagonal and lamellar phases is also evident from the 1D X-ray patterns (Fig. 4E). The 1D XRD patterns of 6 wt% Brij-56-directed silica film without semiconducting polymer guests and with MEH-PPV, PFO, or F8BT incorporated are shown in Fig. 4E, lines i, ii, iii, and iv, respectively. These patterns are in agreement with the 2D SAXS results showing a combination of the hexagonal (100) and (200) reflections with a lattice parameter of  $\sim 5.0$  nm, and the (001) and (002) reflections of the lamellar mesophase with a basal spacing of  $\sim 5.3$  nm. The hexagonal lattice parameters and lamellar basal spacing values of the 6 wt% Brij-56-directed silica films without and with semiconducting polymer guests, calculated from the 1D X-ray patterns in Fig. 4E are listed in Table 1.

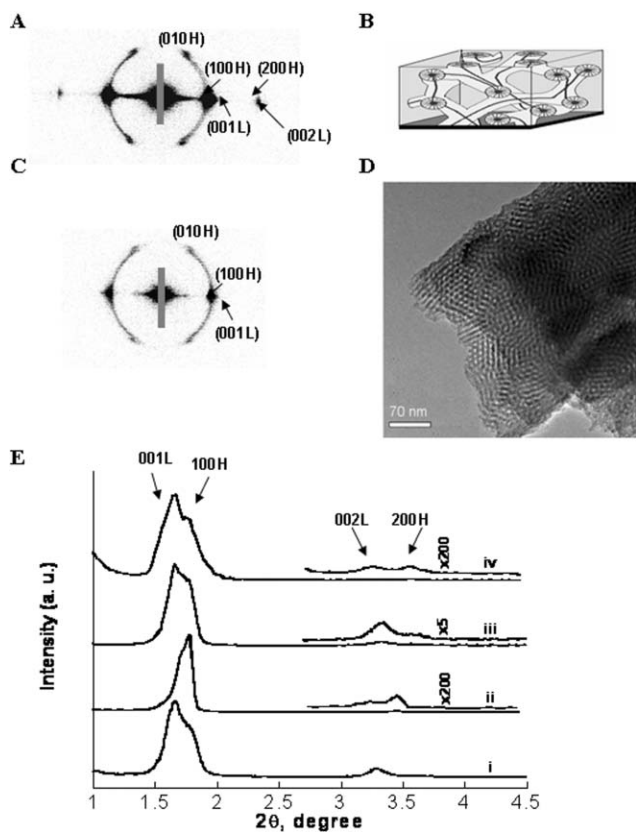


**Fig. 4** (A) The 2D-SAXS pattern of a 6 wt% Brij-56-directed silica nanocomposite film (the film plane is indicated by the vertical grey line as explained in the Experimental). (B) A schematic illustration of the disorder domains of worm-like cylindrical micelles. (C) 2D-SAXS pattern of a 6 wt% Brij-56-directed PFO-incorporated silica nanocomposite film. (D) A TEM image of the 2D hexagonal domains of the 6 wt% Brij-56-directed silica nanocomposite films. (E) 1D X-ray patterns a 6 wt% Brij-56-directed mesostructured silica film (line i), and 6 wt% Brij-56-directed nanocomposite films incorporated with: red-emitting MEH-PPV (line ii), blue-emitting PFO (line iii), and green-emitting F8BT (line iv).

The results presented in Table 1 reveal a hexagonal-to-lamellar phase transition induced by increasing the surfactant concentration in the hydrophobic sol solution. The hexagonal reflections in the X-ray patterns of all 3 wt%-Brij-56-directed films, corresponding to  $d$ -spacing of 5.0–5.14 nm, are still present in the X-ray patterns of all 6 wt%-Brij-56-directed films, but are absent from the X-ray patterns of all 8 wt%-Brij-56-directed films. Accordingly, the lamellar reflections in all 8 wt%-Brij-56-directed films, corresponding to a  $d$ -spacing of 5.3 nm, are noticeable in all X-ray patterns of 6 wt%-Brij-56-directed films, but absent from the 3 wt%-Brij-56-directed film patterns.

The results presented in Table 1 also reveal that incorporating the semiconducting polymers into the hexagonal mesostructure induces a noticeable increase of the  $d$ -spacing by up to 0.14 nm, while incorporation of the conjugated polymers into the lamellar mesostructure results in a minor ( $<0.06$  nm) or no increase of the interlayer spacing.

The main issues in characterizing the conjugated polymer-incorporated hexagonal, lamellar and mixed mesostructured

silica nanocomposite films are whether the conjugated polymers are indeed located in the silica channels, and, if so, the average number of semiconducting polymer chains incorporated in a single channel. Assuming the conjugated polymer chains are positioned in the hydrophobic regions of the surfactant, an effective diameter of 0.6 nm for a given conjugated polymer molecule, and  $\pi$ - $\pi$  interchain distance of  $\sim 0.35$  nm,<sup>50</sup> the 5–6 nm organic core could accommodate up to 6 polymer chains.<sup>25</sup> However, the absence of a significant shift to higher  $d$ -spacing upon incorporation of the conjugated polymers into the structures of both the hexagonal and lamellar nanocomposites, is probably due to the low conjugated polymer loading of the nanocomposite films.

Conjugated polymer loading was estimated by dissolving the films in THF and measuring the solutions absorption spectra and found to be 0.2–1.5 wt%. The conjugated polymer uptake in the films slightly increases with surfactant concentration; *i.e.* polymer loading is highest in the lamellar 8 wt%-Brij-56-directed films, and lowest in the hexagonal 3 wt%-Brij-56-directed films. This result reflects the synthetic conditions where the surfactant–conjugated polymer ratio is maintained constant in all the precursor solutions. However, for the purpose of this discussion we shall assume similar polymer loading in all nanocomposite films due to the small differences in conjugated polymer concentrations in the different precursor solutions and the inaccuracy of polymer loading determination. We speculate that the low loading of conjugated polymers is due to THF evaporation during the EISA process, which causes some polymer sedimentation, leaving a low concentration of conjugated polymer chains associated with the hydrophobic block of the surfactant, to be incorporated into the nanocomposite film.

### Nanocomposite optical properties

The molecular arrangements of semiconducting polymer chains are reflected in their optical absorption spectra. For example, two distinct phases have been identified in the absorption spectra of PFO solutions and films: a glassy phase ( $\alpha$ -phase) and a phase with extended conjugation ( $\beta$ -phase).<sup>51,52</sup> The absorption spectra of PFO solutions and films spun from good solvents show only the broad featureless absorption peak of the glassy  $\alpha$ -phase centered at  $\sim 380$  nm. The absorption spectra of highly concentrated solutions or films spun from moderately good solvents, on the other hand, show also distinct vibronic transitions of the  $\beta$ -phase, in addition to the broad  $\alpha$ -phase peak (Fig. 5A, dashed line). The absorption of the planar extended-conjugation  $\beta$ -phase is red-shifted, compared to that of the glassy  $\alpha$ -phase, with peaks at 400 and 435 nm that are assigned to the 0–1 and 0–0 vibronic transitions, respectively. These  $\beta$ -phase features are a result of *intra*-molecular interactions on planar chain segments, rather than interactions between neighboring chains.<sup>51</sup>

The optical absorption spectra of 3 wt% Brij-56- $\square$ , 6 wt% Brij-56- $\times$ , and 8 wt% Brij-56-(solid lines) directed semiconducting polymer-incorporated mesostructured silica films are shown in Fig. 5 incorporating PFO (Fig. 5A), F8BT (Fig. 5B), or MEH-PPV (Fig. 5C). For comparison, the spectra of pristine films of each conjugated polymer alone are

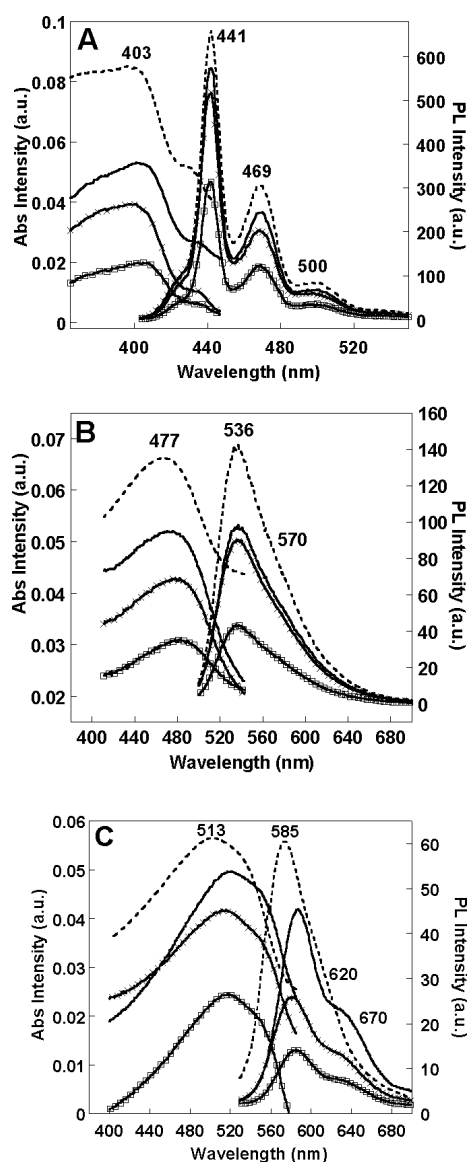


**Fig. 5** Optical absorption and PL spectra of: (A) a PFO pristine polymer film (dashed lines), 3 wt% Brij-56-directed PFO-incorporated mesostructured silica ( $\square$ ), 6 wt% Brij-56-directed PFO-incorporated mesostructured silica (X), and 8 wt% Brij-56-directed PFO-incorporated mesostructured silica (solid lines). (B) An F8BT pristine polymer film (dashed lines), 3 wt% Brij-56-directed F8BT-incorporated mesostructured silica ( $\square$ ), 6 wt% Brij-56-directed F8BT-incorporated mesostructured silica (X), and 8 wt% Brij-56-directed F8BT-incorporated mesostructured silica (solid lines). (C) An MEH-PPV pristine polymer film (dashed lines), 3 wt% Brij-56-directed MEHPPV-incorporated mesostructured silica ( $\square$ ), 6 wt% Brij-56-directed MEHPPV-incorporated mesostructured silica (X), and 8 wt% Brij-56-directed MEHPPV-incorporated mesostructured silica (solid lines).

also presented (dashed lines). In general, the optical absorption spectra of the semiconducting-polymer-incorporated silica films are similar to those of the corresponding pristine conjugated polymer films. Due to the inhomogeneous scattering of light in the visible region by the surfactant-silica matrix ( $\sim 15\%$ ), typical peaks in the absorption spectra of the conjugated polymers could not be accurately assigned in the mesostructured composite films. Nevertheless, the absorption

spectra indicate that the polymers maintain their optical properties when incorporated into the silica matrix. More specifically, the optical absorption spectrum of PFO incorporated in mesostructured silica (Fig. 5A) shows the broad featureless absorption peak of the glassy  $\alpha$ -phase centered at  $\sim 380$  nm, and the 0-1 and 0-0 vibronic transitions of the extended-conjugation  $\beta$ -phase at 400 and 435 nm, respectively.<sup>33,51,52</sup>

The optical absorption of an F8BT film and incorporated F8BT chains (Fig. 5B) show the reported localized transition to the charge-transfer state at  $\sim 477$  nm.<sup>53</sup> The absorption peak in the spectra of MEH-PPV film and MEH-PPV-incorporated nanocomposites (Fig. 5C) is also assigned to the  $\pi$ - $\pi^*$  transition.<sup>54,55</sup>

A major general difference between the optical absorption and photoluminescence (PL) spectra of semiconducting polymers is that while optical absorption reflects the entire population of conjugated polymer chains, the PL spectrum reflects only those chain segments with the lowest band-gap (*i.e.*, highest extent of conjugation). This is a result of the efficient energy transfer that rapidly funnels the excited states (excitons) to the low-gap segments prior to radiative emission.<sup>56</sup> The photoluminescence spectra of the 3 wt% Brij-56- ( $\square$ ), 6 wt% Brij-56- (X), and 8 wt% Brij-56- (solid lines) directed semiconducting polymer-incorporated silica films are also shown in Fig. 5, combined with those of pristine polymer films (dashed lines). The photoluminescence spectra of the semiconducting-polymer-incorporated silica films have similar features to those of the corresponding pristine conjugated polymer films. For example, the photoluminescence of both PFO and PFO-incorporated nanocomposite films (Fig. 5A) show well-resolved vibronic peaks at 440 and 466 nm, and a shoulder at approximately 500 nm, assigned to the 0-0, 0-1 and 0-2 intrachain singlet transitions, respectively.<sup>51,52</sup> The emission spectra of pristine F8BT and F8BT-incorporated silica films (Fig. 5B) are similar showing a broad featureless peak centered at  $\sim 535$  nm, which is composed of two poorly resolved transitions originating from the intrachain exciton strongly coupled to the interchain state.<sup>57,58</sup>

In contrast to PFO and F8BT, the incorporation of MEH-PPV into the mesostructured silica films induced noticeable changes in the polymer PL spectra compared to that of pristine MEH-PPV films. More specifically, the 0-0, 0-1 and 0-2 vibronic transitions in the pristine polymer PL spectrum<sup>54,55</sup> are up to 15 nm red-shifted in the PL spectra of incorporated MEH-PPV, as shown in Fig. 5C. The red-shifted PL spectra indicates that confinement of the flexible MEH-PPV chain into the ordered channels of the silica-surfactant host matrices induces an extended chain morphology, which enhances the conjugation lengths.<sup>23</sup> This coiled-to-extended MEH-PPV chain morphology change, induced by incorporation into the matrix, is not observed for PFO chains because PFO is intrinsically in an extended morphology as evident from its relatively small Stokes shift (difference between absorption and emission maximum peak position). These results are in good agreement with the optical absorption measurements of semiconducting polymers infiltrated into mesoporous silica and titania.<sup>25,26</sup> Extended conjugation increases carrier mobility and is desired for the improvement

of polymer devices, such as light-emitting diodes and field-effect transistors.

Additional properties highly desired for plastic electronics in general, and light-emitting devices specifically, are chemical and environmental stability. The photochemical stability of the PFO incorporated into the silica matrix is investigated by comparing the PL spectra of a pristine PFO film to that of a PFO-incorporated silica nanocomposite film upon exposure to air and white light illumination (Fig. 6A and B, respectively). As reported in the literature, after five weeks of exposure, the PL spectrum of the pristine polymer film shows a significant reduction in the blue emission, and the appearance of a green peak centered at  $\sim 540$  nm (Fig. 6A).<sup>51,52</sup> The PL spectrum of an otherwise identically treated PFO-incorporated 3 wt%-Brij-56-directed silica nanocomposite film, on the other hand, shows that the nanocomposite films maintain their blue emission characteristics, albeit with somewhat reduced intensity, and no green emission is observed (Fig. 6B). Furthermore, the blue emission is preserved in the PFO-incorporated nanocomposite films even after over more than four months at ambient conditions, while the PL spectrum of PFO polymer films stored under identical conditions for the same period of time shows only traces of the broad green peak.

The increased photostability was also observed for the PFO-incorporated 6 and 8 wt%-Brij-56-directed nanocomposite films. The origin of the polyfluorene emission shift from blue to green is attributed to oxidative degradation of PFO units forming on-chain keto-defects (fluorenone sites) emitting in the green.<sup>51,52</sup> Several studies have shown that the oxidation

processes is insufficient to induce the green emission, and intermolecular aggregate–excimer states involving closely stacked PFO and fluorenone defects are necessary.<sup>51,52</sup> Therefore, the increased photo-stability and color purity of the PFO when incorporated into the silica matrix may be attributed to the inhibition of oxidation by blocking the oxygen penetration, combined with hindering exciton migration by reducing interchain interactions. Therefore, the incorporation of conjugated polymers into the silica matrix provides dramatically improved photophysical stability and new opportunities for the design of long-lived organic LED devices, a major objective of polymer-based electronics.

### Nanocomposite-based light-emitting diodes

The fundamental physical process central to the function of organic electroluminescent devices involves the injection of charge carriers from the electrodes into the emissive material and their propagation along conjugated polymer chains to form electron-hole pairs (excitons) that can recombine through emission of a photon.<sup>2,59</sup> The existence of a continuous conductive network providing a carrier pathway between the two electrodes and the recombination of excitons on a conjugated polymer segment is an inherent condition for polymer light-emitting diodes (PLEDs). Consequently, electroluminescence, *i.e.*, light emission under applied bias, is itself indicative of an interconnecting polymer network that spans between the cathode and anode of the PLED. In semiconducting polymer–silica films, a conductive polymer pathway can result from macrophase separation of large polymer aggregates contacting the two electrodes. Indeed, PLEDs comprising blends of semiconducting polymers and silica have shown diode characteristics and light emission due to the formation of large semiconducting polymer domains in the silica film.<sup>60</sup> In the case of semiconducting polymer-incorporated mesostructured silica, however, we expect the device performance to be dependent on the orientation and connectivity of the hydrophobic channels hosting the semiconducting polymers. If the hydrophobic channels form a continuous cathode-to-anode network, then charges can be transported along the semiconducting polymers in these regions and recombine radiatively. However, if the hydrophobic channels do not connect the two electrodes, then insulating silica layers will act as barriers to charge transport, so that no light emission is expected. Therefore, electroluminescence, in combination with the X-ray diffraction and optical measurements, can be used to deduce the location of the semiconducting polymer in the composite materials.

Polymer light-emitting diodes based on 2D hexagonal, cylindrical worm-like, cubic or lamellar mesostructured silica nanocomposites containing different conjugated polymers were fabricated and their performance metrics measured and compared. The general PLED device structure was: ITO–hole-injecting-layer–nanocomposite–Ca–Al, as shown in Fig. 7A. The JVL (current density–voltage–luminance) characteristics and electroluminescence spectra of the conjugated polymer-incorporated 3, 6 or 8 wt% Brij-56–silica nanocomposite light-emitting diodes (LEDs) are shown in Fig. 7B–C (PFO-incorporated), Fig. 7D–E (F8BT-incorporated) and

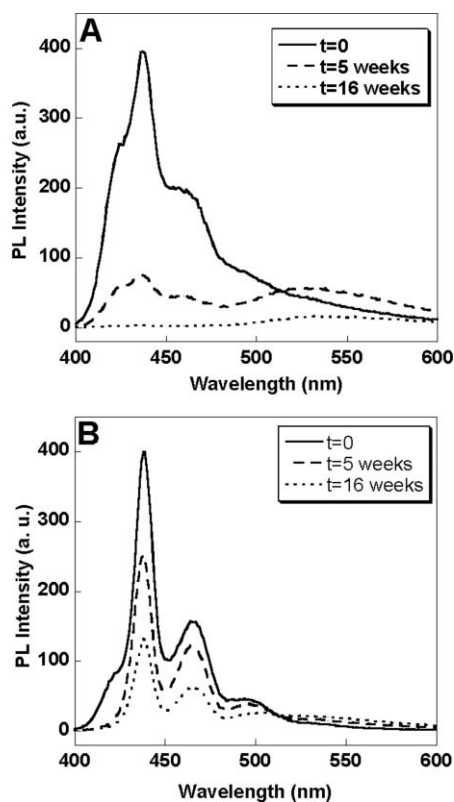
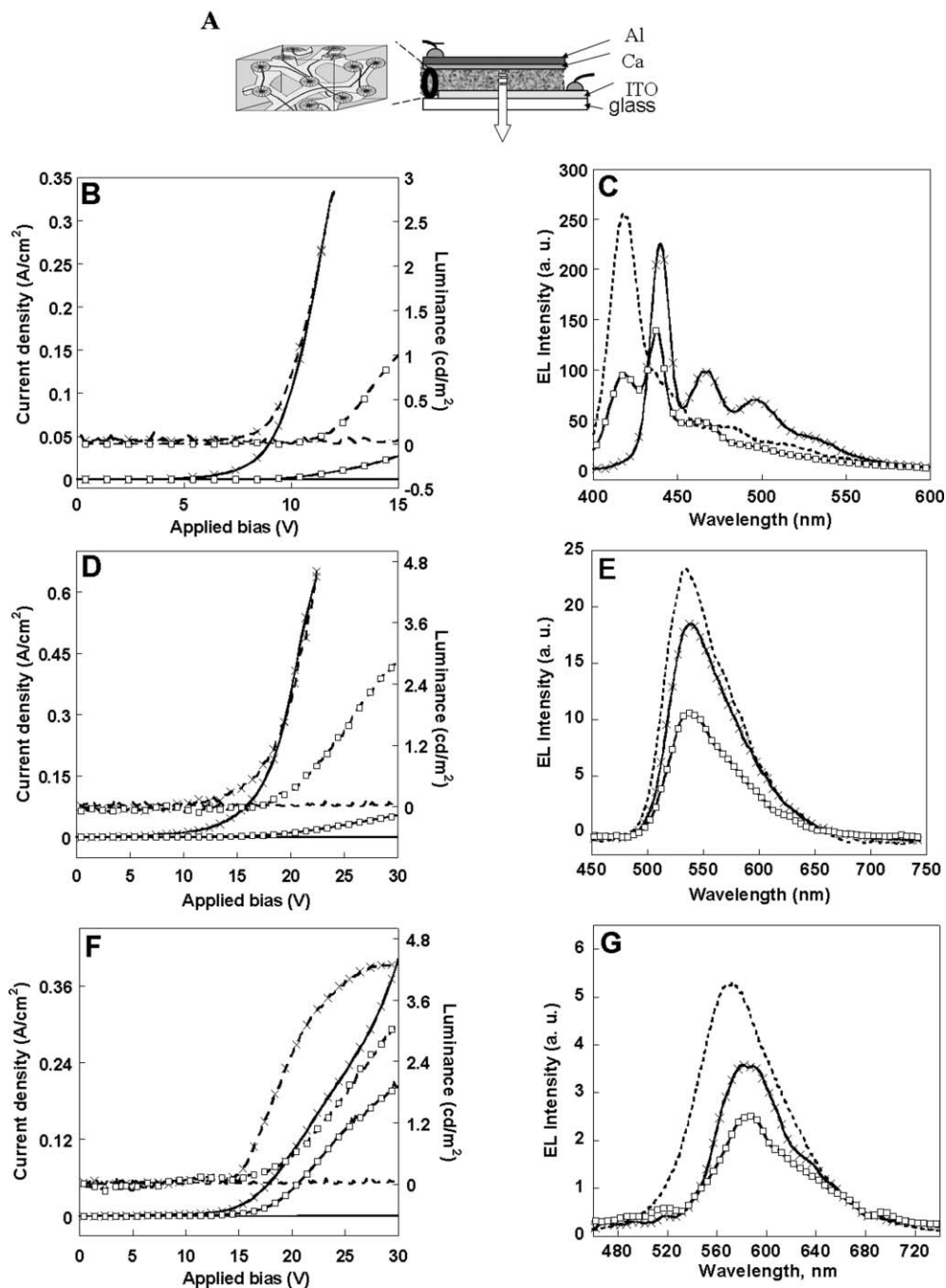


Fig. 6 The PL spectra of (A) a pristine PFO film; and (B) a 3 wt% Brij-56-directed PFO-incorporated silica nanocomposite film, as a function of time stored in air and exposed to white light.

Fig. 7F–G (MEH-PPV-incorporated). Devices based on the oriented lamellar conjugated-polymer-incorporated–8 wt% Brij-56–silica nanocomposites showed weak or no diode behavior and no light emission at all. In contrast, devices based of structures composed of a mixture of 2D hexagonal, cylindrical worm-like and cubic phases, deposited from the 3 or 6 wt% Brij-56–sol solutions exhibited typical diode behavior and light emission.

As previously mentioned, all 3 and 6 wt% Brij-56-directed silica nanocomposite films contain a mixture of ordered 2D hexagonal domains oriented parallel to the substrate, and a significant amounts of disordered worm-like domains, as indicated by strong diffraction arcs superimposed on the hexagonal spots in the 2D-SAXS patterns. Depending on film processing conditions, the 3 wt% Brij-56-directed silica nanocomposite films can also include ordered 3D-cubic



**Fig. 7** (A) A schematic representation of the general light-emitting device structure with a disordered worm-like phase as the active layer: ITO–PEDOT:PSS–{semiconducting polymer-incorporated-Brij-56-silica}–Ca–Al. (B), (D), and (F): current density (solid lines)–voltage–luminance (dashed lines) characteristics of devices based on conjugated polymer-incorporated 3 wt% (□), 6 wt% (X), and 8 wt% (no mark) Brij-56-directed silica films: PFO (B), F8BT (D), and MEHPPV (F). (C), (E), and (G) EL spectra of devices based on conjugated polymer-incorporated 3 wt% (□), and 6 wt% (X) Brij-56-directed silica films, and pristine polymer films (dashed lines): PFO (C), F8BT (E), and MEHPPV (G).

domains; while the 6 wt% Brij-56-directed silica nanocomposite lamellar domains, respectively. In contrast, the 8 wt%-Brij-56-directed silica nanocomposite films consist of the lamellar structure, only, regardless of film-processing conditions.

Accordingly, we attribute the LED behavior of the semi-conducting polymer PFO-, F8BT- and MEH-PPV-incorporated 3 and 6 wt% Brij-56 directed-silica nanocomposites to the interpenetrating continuous conjugated polymer network between the two electrodes provided by the worm-like disordered regions, coexisting with the 2D-hexagonal and 3D-cubic phases. In contrast, in the lamellar silica mesocomposite films, the conjugated polymer chains extend parallel to and are largely insulated from the electrodes by the silica sheets. As a consequence, the conjugated polymer chains do not form a continuous network through the film between the electrodes and thus the lamellar mesocomposite shows no LED performance whatsoever. The dramatic differences in the performance of diodes prepared from the different phases indicate that the conjugated polymer species are indeed incorporated in the ordered hydrophobic channels of the nanocomposite host matrix and are neither macroscopically phase-separated nor distributed randomly within the nano-structured silica films.

The performance of the conjugated polymer-incorporated 3 and 6 wt% Brij-56-silica nanocomposite light-emitting diodes are poorer than those of pristine polymer films as summarized in Table 2. The high fields required for current and light turn-on in the nanocomposite devices are due to the insulating character of the silica host matrix, which inhibits charge transfer, and suggest that carriers are injected from the electrodes into a thin composite layer adjacent to the electrode, followed by carrier transport mainly along the polymer chains and recombination on emissive polymer segments. The much lower brightness observed for the nanocomposite devices compared to those of a simple pristine conjugated polymers PLEDs<sup>2,58,61</sup> are the result of the very low polymer content in the composite film, further limited by abundance of hexagonal or lamellar domains in the film. This suggestion is further supported by comparing the LED performances of the 3 wt% Brij-56 directed nanocomposite films to those of the 6 wt% Brij-56 directed nanocomposite films. As mentioned earlier, the conjugated polymer uptake in the nanocomposite

films corresponds directly to the surfactant concentration, and hence is higher in the in 6 wt% Brij-56 directed nanocomposite films than in the 3 wt% Brij-56 directed nanocomposite films. Consequently, the turn-on voltages, current densities and brightness of the 6 wt% Brij-56 directed films are higher than those of the corresponding 3 wt% Brij-56 directed films (Fig. 7 and Table 2), regardless of the type of conjugated polymer incorporated. We conclude therefore, that the nanocomposites device performance is currently limited by the low conjugated polymer loading and only partial presence of interpenetrating disordered worm-like regions, hence a substantial increase in conjugated polymer up-take is expected to provide long-lived, highly luminescent LEDs.

The electroluminescence spectra of the F8BT and MEH-PPV-incorporated 3 and 6 wt% Brij-56 directed nanocomposites (Fig. 7) generally resemble their corresponding PL spectra (Fig. 5), and the PL and EL spectra of pristine polymer films (Fig. 5 and Fig. 7). For example, the EL spectra of F8BT-incorporated silica nanocomposites (Fig. 7E) exhibit the strong broad peak at 534 nm and shoulder at 570 nm, also observed in the nanocomposite PL spectra (Fig. 5B) and the EL spectrum of pristine F8BT diodes (Fig. 7E). PFO-incorporation into the silica matrix, on the other hand, induced noticeable changes in the EL spectra compared to that of pristine PFO films. The EL spectrum of a spun pristine PFO diode exhibits a strong emission peak from the disordered  $\alpha$ -phase chains centered at  $\sim$ 420 nm, and weaker shoulders at 440, 476 and 500 nm assigned to the 0-0, 0-1, and 0-2 transitions from  $\beta$ -phase aggregates, respectively (Fig. 7C). In contrast to the EL spectrum of pristine polymer films, the EL spectra of the PFO-incorporated nanocomposite are dominated by the extended  $\beta$ -phase transitions. The  $\alpha$ -phase transition is still noticeable in the EL spectrum of the PFO-incorporated 3 wt% Brij-56 directed silica nanocomposite diode (Fig. 7C), but diminished in the EL spectrum of the higher conjugated polymer loaded 6 wt% Brij-56 directed nanocomposites (Fig. 7C). We conclude therefore, that incorporation of the PFO chains into the nanocomposites induces an extended chain morphology and polymer aggregation in the silica channels. Aggregation of the incorporated conjugated polymer chains in the silica channels is also evident from the red-shifted photoluminescence (Fig. 5B and 5C) and electroluminescence (Fig. 7E and 7G) spectra of MEH-PPV-incorporated silica

**Table 2** JVL characteristics of nanocomposite and pristine polymer light-emitting diodes averaged over 12 devices of each type. The standard deviations of nanocomposite device turn-on voltage, luminance and current density were < 8%, 25% and 30%, respectively

Material	$V_{\text{turn on}}, V$	Luminance/cd m <sup>-2</sup>	Current density/A m <sup>-2</sup>
Pristine PFO	3.3	20 (at 6.5 V)	4 (at 6.5 V)
PFO-3 wt% Brij-silica	10	1.2 (at 16 V)	0.03 (at 16 V)
PFO-6 wt% Brij-silica	8	3.0 (at 12 V)	0.35 (at 12 V)
PFO-8 wt% Brij-silica	—	—	—
Pristine F8BT	3.6	14 (at 7 V)	3.8 (at 7 V)
F8BT-3 wt% Brij-silica	18.5	2.8 (at 30 V)	0.05 (at 30 V)
F8BT-6 wt% Brij-silica	15.5	4.6 (at 23 V)	0.65 (at 23 V)
F8BT-8 wt% Brij-silica	—	—	—
Pristine MEH-PPV	4.3	13 (at 8 V)	4.2 (at 8 V)
MEH-PPV-3 wt% Brij-silica	18.2	3.1 (at 30 V)	0.21 (at 30 V)
MEH-PPV-6 wt% Brij-silica	16	4.3 (at 30 V)	0.4 (at 30 V)
MEH-PPV-8 wt% Brij-silica	—	—	—
PFO-3 wt% PEO-silica	5.6	5.5 (at 8 V)	0.7 (at 8 V)
PFO-6 wt% PEO-silica	4.2	7.6 (at 8 V)	0.8 (at 8 V)
PFO-8 wt% PEO-silica	3.7	7.7 (at 8 V)	0.8 (at 8 V)

nanocomposite films compared to those of the corresponding pristine polymer films.

To confirm that the mesostructured nanocomposite device behavior is governed by the conjugated polymer chains that are incorporated in the hydrophobic channels of the mesostructure, and not by conjugated polymer domains macroscopically phase-separated in the film, the structure-directing surfactant in the precursor solution is replaced with a non-structure-directing polymer: poly(ethylene oxide) (PEO). PEO is selected because it represents the hydrophilic block of the surfactant Brij-56, but with the absence of the hydrophobic block and therefore can not induce the formation of micelles and liquid-crystalline phases. Consequently, replacing Brij-56 with PEO in the sol solution is expected to promote the formation of macrophase-separated conjugated polymer domains in a PEO-silica film. Comparing the optical and opto-electronic properties of the disordered conjugated polymer-PEO-silica films with those of the corresponding conjugated polymer incorporated-Brij-56-directed silica nanocomposites, provides the means to associate the device performance with either incorporated polymer chains, or phase-separated polymer domains.

The presence of PFO domains in the films deposited using the synthetic protocol developed for the deposition of conjugated polymer-incorporated mesostructured silica, but replacing Brij-56 with PEO, is evident from their optical absorption and photoluminescence spectra. The absorption spectra of the PFO-PEO-silica film (ESI†) are noticeably red-shifted, >10 nm, compared to the absorption spectra of a pristine PFO film and to PFO-incorporated Brij-56-directed silica films (Fig. 5A), associated with the increased conjugation length of PFO chains in aggregated domain. The PL spectra of PFO-PEO-silica films provide further evidence for PFO aggregation reflected in the relative intensities of the 440 and 466 nm peaks. The aggregation of PFO chains induces interchain emission bands that overlap with the principal intramolecular exciton emission and increase the PL intensity in the 470–500 nm range.<sup>62</sup> The reduced relative intensity of the 440 and 466 nm peaks in the PL spectrum of the PFO-8 wt% PEO-silica films (Fig. 8) compared to that in the PL spectra of pristine PFO films and all mesostructured

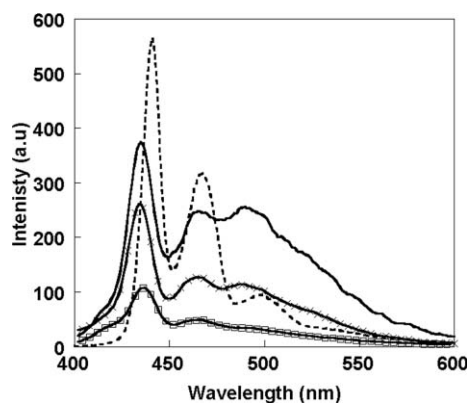


**Fig. 8** The PL spectrum of a PFO-8 wt% PEO-silica nanocomposite film (dashed line), and EL spectra of PFO/3 wt% ( $\square$ ), 6 wt% ( $\times$ ) and 8 wt% (solid line) PEO-silica LEDs.

PFO-incorporated silica films (Fig. 5A) reflects the contributions of aggregate transitions in PFO-PEO-silica PL spectrum. Similar intermolecular transitions were also observed in the PL spectra of PFO-3 and 6 wt% PEO-silica films, indicating that blending PEO, silica and PFO results in the formation of large PFO aggregates. The significant differences between the optical properties of PFO-PEO-silica and PFO-Brij-56-silica films corroborate that the conjugated polymer chains are incorporated into the hydrophobic channels of the surfactant-directed mesostructured silica and not macrophase-separated into polymer domains in the silica matrix.

Diodes based on the PFO-PEO-silica films all showed diode behavior and light-emission regardless of the PEO concentration, in contrast to the Brij-56-directed mesostructured nanocomposite devices, where the device performance was crucially dependant on the Brij-56 surfactant concentration. Representative JVL characteristics and EL spectra of the PFO-PEO-silica diodes are listed in Table 2 and shown in Fig. 8, respectively. The reduced turn-on voltages and improved current densities and brightness of the PFO-PEO-silica devices compared to the corresponding mesostructured films are assigned to the presence of large polymer aggregates in the silica matrix, which provide continuous and efficient charge-transport routes through the film. Accordingly, the device characteristics improve with increasing PEO concentration (and hence PFO concentration, because the PEO-PFO concentration ratio is kept constant between all samples) approaching the performance of a pristine PFO LED. The electroluminescence spectra of the disordered PFO-PEO-silica films are also dominated by the presence of large conjugated polymer domains, with an increased contribution of the aggregate transitions at 470–500 nm, similarly to that observed in their PL spectra (Fig. 8). The striking optical and opto-electronic differences between the PEO-PFO-silica blends and the PFO-incorporated Brij-56-directed silica nanocomposites confirm that the self-organization of the surfactant leads to the inclusion of the conjugated polymer species in the hydrophobic channels of the silica, while the surfactants hydrophilic segments template the polymerization of silica in liquid-crystalline phases. The continuous network of semiconducting polymer species throughout the 3 and 6% Brij-56-directed silica films enabled the integration of ordered nanocomposites into electronic devices.

A continuous conjugated polymer network could also form through defects in the silica walls of the mesostructures. Porous defects are known to exist in the thin silica walls of calcined Brij-56-directed 2D-hexagonal films ( $\sim 1$  nm), as demonstrated by high  $N_2$  gas adsorption uptake.<sup>45</sup> But, formation of the continuous polymer-threaded defect network is not likely to form through the film thickness. Therefore, intentionally directing a phase with continuous through-film conductive pathway has allowed the integration of ordered semiconducting polymer-silica nanocomposites into opto-electronic devices.

## Conclusions

In conclusion, optimization of materials synthesis chemistries and mesophase self-assembly processes, allow new hierarchical

structures of mesostructured silica–surfactant–semiconducting polymer nanocomposites to be tailored for electronic and opto-electronic applications. Incorporation of the semiconducting polymers into an inorganic matrix can not only endow the polymer with improved environmental and chemical stability, but might also induce beneficial properties for desired applications such as polarized emission. According to the selection of different surface-active agents, inorganic precursor species, conjugated polymer solutes, and, crucially, mutually compatible non-aqueous solvents, it was possible to prepare preferentially 2D hexagonally ordered or lamellar mesophase silica with semiconducting polymer guest species incorporated within the hydrophobic channels. The continuous network of semiconducting polymer species throughout the silica mesostructure enabled the integration of ordered nanocomposites into electronic devices. This was demonstrated by the separate fabrication of red, green, or blue nanocomposite LEDs comprising blue PFO-, green F8BT-, or red MEH-PPV polymer-incorporated partially aligned silica mesostructures. The nanocomposite device performance is currently limited by the low conjugated polymer loading and only partial presence of active interpenetrating disordered worm-like regions in the film. A substantial increase of the conjugated polymer uptake into a worm-like or cubically-ordered film, with continuous through-film organic and inorganic networks, is expected to yield long-lived, highly luminescent LEDs. The non-aqueous approach presented here for the preparation of optically responsive semiconducting polymer-incorporated mesostructured inorganic host matrices is expected to be general and extendable to other hybrid material compositions and structures.

## Acknowledgements

This project was funded by the United States–Israel Binational Science Foundation, grant number 2002134. GLF is a Landau Fellow, supported by the Taub and Shalom Foundations. CJB is supported through DOE Basic Energy Sciences, AFOSR and ARO.

## References

- 1 J. H. Burroughes, D. D. C. Bradley, A. R. Brown, R. N. Marks, K. Mackay, R. H. Friend, P. L. Burns and A. B. Holmes, *Nature*, 1990, **347**, 539.
- 2 R. H. Friend, R. W. Gymer, A. B. Holmes, J. H. Burroughes, R. N. Marks, C. Taliani, D. D. C. Bradley, D. A. Dos Santos, J. L. Bredas, M. Logdlund and W. R. Salaneck, *Nature*, 1999, **397**, 121.
- 3 G. Horowitz, *Adv. Mater.*, 1998, **10**, 365.
- 4 C. D. Dimitrakopoulos and P. R. L. Malenfant, *Adv. Mater.*, 2002, **14**, 99.
- 5 M. D. McGehee and A. J. Heeger, *Adv. Mater.*, 2000, **12**, 1655.
- 6 J. J. M. Halls, C. A. Walsh, N. C. Greenham, E. A. Marseglia, R. H. Friend, S. C. Moratti and A. B. Holmes, *Nature*, 1995, **376**, 498.
- 7 K. M. Coakley and M. D. McGehee, *Chem. Mater.*, 2004, **16**, 4533.
- 8 G. Yu, J. Gao, J. C. Hummelen, F. Wudl and A. J. Heeger, *Science*, 1995, **270**, 1789.
- 9 F. Mammeri, E. Le Bourhis, L. Rozes and C. Sanchez, *J. Mater. Chem.*, 2005, **15**, 3787.
- 10 E. Bourgeat-Lami, *J. Nanosci. Nanotechnol.*, 2002, **2**, 1.
- 11 H. Colfen and S. Mann, *Angew. Chem., Int. Ed.*, 2003, **42**, 2350.
- 12 C. Sanchez, B. Julian, P. Belleville and M. Popall, *J. Mater. Chem.*, 2005, **15**, 3559.

- 13 R. Gangopadhyay and A. De, *Chem. Mater.*, 2000, **12**, 2064.
- 14 C. O. Oriakhi, *J. Chem. Educ.*, 2000, **77**, 1138.
- 15 C. Sanchez, B. Lebeau, F. Chaput and J. P. Boilot, *Adv. Mater.*, 2003, **15**, 1969.
- 16 B. Dunn and J. I. Zink, *Sol-Gel Technol. Glass Prod. Users*, 2004, 355.
- 17 P. N. Minoofar, R. Hernandez, S. Chia, B. Dunn, J. I. Zink and A. C. Franville, *J. Am. Chem. Soc.*, 2002, **124**, 14388.
- 18 R. Hernandez, A. C. Franville, P. Minoofar, B. Dunn and J. I. Zink, *J. Am. Chem. Soc.*, 2001, **123**, 1248.
- 19 T. Keeling-Tucker and J. D. Brennan, *Chem. Mater.*, 2001, **13**, 3331.
- 20 N. A. Melosh, C. A. Steinbeck, B. J. Scott, R. C. Hayward, P. Davidson, G. D. Stucky and B. F. Chmelka, *J. Phys. Chem. B*, 2004, **108**, 11909.
- 21 P. D. Yang, G. Wirnsberger, H. C. Huang, S. R. Cordero, M. D. McGehee, B. Scott, T. Deng, G. M. Whitesides, B. F. Chmelka, S. K. Buratto and G. D. Stucky, *Science*, 2000, **287**, 465.
- 22 T. D. de Morais, F. Chaput, K. Lahlil and J. P. Boilot, *Adv. Mater.*, 1999, **11**, 107.
- 23 T. Q. Nguyen, J. J. Wu, V. Doan, B. J. Schwartz and S. H. Tolbert, *Science*, 2000, **288**, 652.
- 24 T. Q. Nguyen, J. Wu, S. H. Tolbert and B. J. Schwartz, *Adv. Mater.*, 2001, **13**, 609.
- 25 J. J. Wu, A. F. Gross and S. H. Tolbert, *J. Phys. Chem. B*, 1999, **103**, 2374.
- 26 K. M. Coakley, Y. X. Liu, M. D. McGehee, K. L. Frindell and G. D. Stucky, *Adv. Funct. Mater.*, 2003, **13**, 301.
- 27 Y. F. Lu, Y. Yang, A. Sellinger, M. C. Lu, J. M. Huang, H. Y. Fan, R. Haddad, G. Lopez, A. R. Burns, D. Y. Sasaki, J. Shelnutt and C. J. Brinker, *Nature*, 2001, **410**, 913.
- 28 A. G. Pattantyus-Abraham and M. O. Wolf, *Chem. Mater.*, 2004, **16**, 2180.
- 29 M. Alvaro, A. Corma, B. Ferrer, M. S. Galletero, H. Garcia and E. Peris, *Chem. Mater.*, 2004, **16**, 2142.
- 30 B. McCaughey, C. Costello, D. H. Wang, J. E. Hampsey, Z. Z. Yang, C. J. Li, C. J. Brinker and Y. F. Lu, *Adv. Mater.*, 2003, **15**, 1266.
- 31 Y. F. Lu, R. Ganguli, C. A. Drewien, M. T. Anderson, C. J. Brinker, W. L. Gong, Y. X. Guo, H. Soyeyz, B. Dunn, M. H. Huang and J. I. Zink, *Nature*, 1997, **389**, 364.
- 32 C. J. Brinker, Y. F. Lu, A. Sellinger and H. Y. Fan, *Adv. Mater.*, 1999, **11**, 579.
- 33 M. Grell, D. D. C. Bradley, X. Long, T. Chamberlain, M. Inbasekaran, E. P. Woo and M. Soliman, *Acta Polym.*, 1998, **49**, 439.
- 34 T. Q. Nguyen, V. Doan and B. J. Schwartz, *J. Chem. Phys.*, 1999, **110**, 4068.
- 35 M. Voigt, J. Chappell, T. Rowson, A. Cadby, M. Geoghegan, R. A. L. Jones and D. G. Lidzey, *Org. Electron.*, 2005, **6**, 35.
- 36 D. Grosso, F. Cagnol, G. J. D. A. Soler-Illia, E. L. Crepaldi, H. Amenitsch, A. Brunet-Bruneau, A. Bourgeois and C. Sanchez, *Adv. Funct. Mater.*, 2004, **14**, 309.
- 37 K. Valle, P. Belleville, F. Pereira and C. Sanchez, *Nat. Mater.*, 2006, **5**, 107.
- 38 R. C. Hayward, P. C. A. Alberius, E. J. Kramer and B. F. Chmelka, *Langmuir*, 2004, **20**, 5998.
- 39 D. Zhao, P. Yang, N. Melosh, J. Feng, B. F. Chmelka and G. D. Stucky, *Adv. Mater.*, 1998, **10**, 1380.
- 40 T. Lee, O. Park, J. Kim, J. Hong and Y. Kim, *Chem. Mater.*, 2001, **13**, 2217.
- 41 J. H. Park, Y. T. Lim, O. Park O, J. K. Kim, J. W. Yu and Y. C. Kim, *Adv. Funct. Mater.*, 2004, **14**, 377.
- 42 E. Aharon, A. Albo, M. Kalina and G. L. Frey, *Adv. Funct. Mater.*, 2006, **16**, 980.
- 43 M. Klotz, P. A. Albouy, A. Ayrat, C. Menager, D. Grosso, A. Van der Lee, V. Cabuil, F. Babonneau and C. Guizard, *Chem. Mater.*, 2000, **12**, 1721.
- 44 P. C. A. Alberius, K. L. Frindell, R. C. Hayward, E. J. Kramer, G. D. Stucky and B. F. Chmelka, *Chem. Mater.*, 2002, **14**, 3284.
- 45 B. Smarsly, A. Gibaud, W. Ruland, D. Sturmayer and C. J. Brinker, *Langmuir*, 2005, **21**, 3858.

- 46 D. A. Doshi, A. Gibaud, V. Goletto, M. C. Lu, H. Gerung, B. Ocko, S. M. Han and C. J. Brinker, *J. Am. Chem. Soc.*, 2003, **125**, 11646.
- 47 A. Gibaud, D. Grosso, B. Smarsly, A. Baptiste, J. F. Bardeau, F. Babonneau, D. A. Doshi, Z. Chen, C. J. Brinker and C. Sanchez, *J. Phys. Chem. B*, 2003, **107**, 6114.
- 48 D. Grosso, F. Babonneau, C. Sanchez, G. J. D. A. Soler-Illia, E. L. Crepaldi, P. A. Albouy, H. Amenitsch, A. R. Balkenende and A. Brunet-Bruneau, *J. Sol-Gel Sci. Technol.*, 2003, **26**, 561.
- 49 E. L. Crepaldi, G. J. D. A. Soler-Illia, A. Bouchara, D. Grosso, D. Durand and C. Sanchez, *Angew. Chem., Int. Ed.*, 2003, **42**, 347.
- 50 C. Y. Yang, F. Hide, M. A. Diaz-Garcia, A. J. Heeger and Y. Cao, *Polymer*, 1998, **39**, 2299.
- 51 S. Gamerith, C. Gadermaier, U. Scherf and E. J. W. List, *Phys. Status Solidi A*, 2004, **201**, 1132.
- 52 D. Neher, *Macromol. Rapid Commun.*, 2001, **22**, 1365.
- 53 K. G. Jespersen, W. J. D. Beenken, Y. Zaushitsyn, A. Yartsev, M. Andersson, T. Pullerits and V. Sundstrom, *J. Chem. Phys.*, 2004, **121**, 12613.
- 54 P. Wood, I. D. W. Samuel, G. R. Webster and P. L. Burn, *Synth. Met.*, 2001, **119**, 571.
- 55 M. Zheng, F. L. Bai and D. B. Zhu, *Polym. Adv. Technol.*, 1999, **10**, 476.
- 56 J. L. Bredas, D. Beljonne, V. Coropceanu and J. Cornil, *Chem. Rev.*, 2004, **104**, 4971.
- 57 C. L. Donley, J. Zaumseil, J. W. Andreasen, M. M. Nielsen, H. Sirringhaus, R. H. Friend and J. S. Kim, *J. Am. Chem. Soc.*, 2005, **127**, 12890.
- 58 J. S. Kim, R. H. Friend, I. Grizzi and J. H. Burroughes, *Appl. Phys. Lett.*, 2005, **87**, 023506/1.
- 59 K. J. Reynolds, J. A. Barker, N. C. Greenham, R. H. Friend and G. L. Frey, *J. Appl. Phys.*, 2002, **92**, 7556.
- 60 J. H. Park, S. Kim, Y. C. Kim and O. O. Park, *Nanotechnology*, 2005, **16**, 1793.
- 61 A. P. Kulkarni and S. A. Jenekhe, *Macromolecules*, 2003, **36**, 5285.
- 62 P. K. H. Ho, J. S. Kim, N. Tessler and R. H. Friend, *J. Chem. Phys.*, 2001, **115**, 2709.



## Looking for that **special** chemical science research paper?

TRY this free news service:

### Chemical Science

- highlights of newsworthy and significant advances in chemical science from across RSC journals
- free online access
- updated daily
- free access to the original research paper from every online article
- also available as a free print supplement in selected RSC journals.\*

\*A separately issued print subscription is also available.

Registered Charity Number: 207890

22030682

RSC Publishing

[www.rsc.org/chemicalscience](http://www.rsc.org/chemicalscience)